Luminescence Diffusion Tomography

Jenghwa Chang[1], Harry L. Graber[2], Randall L. Barbour[1,2]
Department of Pathology[1] and Department of Physiology and Biophysics[2], SUNY Health Science
Center at Brooklyn, Brooklyn, NY 11203, TEL: 718-270-1286, FAX: 718-270-3313

Abstract

Image operators are derived for luminescence diffusion tomography with time–harmonic sources, from a set of coupled radiation transport equations. Simulations and experiments were performed and reconstructed images are presented.

Keywords: Imaging system, Medical and biological imaging, Spectroscopy-fluorescence and luminescence, Optical diagnostics for medicine.

1. Introduction

The use of perturbation methods for optical imaging of tissues using tomographic illumination and detection schemes has attracted significant and increasing interest in recent years [1,2]. This approach involves applying the difference between measurements obtained at the boundary of reference and test media to reconstruct differences between the media's cross sections. The difference signal is usually very small relative to the two quantities being compared, and is sensitive to noise. Use of luminescent light for optical imaging of tissues [3-5], on the other hand, has several important advantages. Luminescence measurements are intrinsically more sensitive than absorption/scattering measurements because in the absence of the lumiphore, the reference intensity is zero. The physical properties of a lumiphore can be sensitive to its immediate chemical environment, and thus provide functional information about the tissue. In addition, by linking the lumiphore to a targeting vehicle (*e.g.*, a monoclonal antibody), the luminescence tomography method becomes similar to radioscintigraphic imaging methods but without the need for exposure to ionizing radiation.

In this paper, we study the excitation and emission in the luminescence phenomenon using two coupled one–speed transport equations. The governing equation describing the fractional excited state lumiphore concentration was also studied. We derived an imaging operator based on transport theory. The final form of this operator is a system of linear equations which can be easily solved by iterative methods. Numerical simulations were performed to calculate this operator using the diffusion equation for a specific test medium. Experimental data were collected using a CT–type scanning laser system. Image reconstructions were performed using a conjugate gradient descent (CGD) [6] algorithm.

2. Theory

The excitation light and emission light associated with a luminescence process are governed by a set of coupled time–dependent radiative transfer equations (RTE) [7,8]:

$$\frac{1}{c}\frac{d\phi_1}{dt} + \Omega \cdot \nabla\phi_1 + \left(\mu_{T,1} + \mu_{T,1\to 2}\right)\phi_1$$
$$= q_1 + \int_{4\pi} \mu_{s,1}(\Omega' \cdot \Omega)\phi_1' \, d\Omega', \tag{1}$$

$$\frac{1}{c}\frac{d\phi_2}{dt} + \Omega \cdot \nabla\phi_2 + \mu_{T,2}\phi_2$$
$$= q_2 + \int_{4\pi} \mu_{s,2}(\Omega' \cdot \Omega)\phi_2' \, d\Omega', \tag{2}$$

where: the subscripts 1 and 2 denote, respectively, the excitation and emitted light (if there is not significant overlap of the absorption and emission spectrum, we can consider only a single frequency in the emission spectrum without loss of generality, as in that case all Equations (2) are coupled with Eq. (1) but not with each other); c is the speed of light; $d\Omega$ is the differential solid angle [sr]; ϕ_1 and ϕ_2 are the angular intensities [$cm^{-2}\ s^{-1}\ sr^{-1}$]; q_1 and q_2 are the angular source strengths [$cm^{-3}\ s^{-1}\ sr^{-1}$]; $\mu_s(\Omega'\cdot\Omega)$ is the macroscopic differential scattering cross section [$cm^{-1}\ sr^{-1}$]; μ_T is the macroscopic total cross section [cm^{-1}]; $\mu_{T,1\rightarrow2} = N_g\Sigma_{T,1\rightarrow2}$ is the change in total cross section after the lumiphore is added, where $\Sigma_{T,1\rightarrow2}$ is the microscopic total cross section [cm^2] of the lumiphore and N_g is the concentration of lumiphore in the electronic ground state. This last quantity, in turn, is governed by

$$\frac{dN_g}{dt} = -\Sigma_{T,1\rightarrow2}\overline{\phi}_1 N_g + \frac{1}{\tau}N_s,\qquad(3)$$

where $N_s = N_0 - N_g$ is the concentration of excited lumiphore, N_0 is the total lumiphore concentration (ground and excited electronic states), $\overline{\phi}_1 = \int_{4\pi}\phi_1 d\Omega$ is the intensity [$cm^{-2}\ s^{-1}$] of the excitation light and τ is the mean lifetime of the luminescent probe's excited state [s]. Thus, the emission source term q_2 in Eq. (2) is

$$q_2 = \frac{\gamma}{4\pi\tau}N_s\qquad(4)$$

where γ is the quantum yield. Let R be the time-domain reading of a given detector for the emitted intensity, and r_2 be the detector sensitivity function. Then

$$R = \int_V\int_{4\pi}r_2\otimes\left(\int_{V'}\int_{4\pi}q_2'\otimes\right.$$

$$\left.G_2(\mathbf{r},\Omega;\mathbf{r}',\Omega';t)d\Omega'd^3r'\right)d\Omega d^3r$$

$$= \int_V\frac{\gamma}{4\pi\tau}N_s\otimes\overline{\phi}_2^+ d^3r,\qquad(5)$$

where the $\otimes$ symbol denotes a convolution in time, N_s is the lumiphore concentration in the excited state,

$G_2(\mathbf{r},\Omega;\mathbf{r}',\Omega';t)$ is the Green's function at $\mathbf{r}$ in direction Ω with the source located at $\mathbf{r}'$ in direction Ω', and

$$\overline{\phi}_2^+ = \int_{4\pi}\int_{V'}\int_{4\pi}r_2'\otimes G_2(\mathbf{r},-\Omega;\mathbf{r}',-\Omega';t)d\Omega'd^3r'd\Omega$$

is the adjoint intensity, which can be interpreted as the intensity at $\mathbf{r}$ arising from a source located at $\mathbf{r}'$. The response frequency-domain detector readings are obtained by Fourier transforming Eq. (5):

$$\widetilde{R} = \int_V\frac{\gamma}{4\pi\tau}\widetilde{N}_s\widetilde{\overline{\phi}}_2^+ d^3r,\qquad(6)$$

where "~" denotes the Fourier transform. Then the Fourier transforms of N_g and N_s are:

$$j\omega\tau\widetilde{N}_g = -\frac{\tau\Sigma_{T,1\rightarrow2}}{2\pi}\widetilde{\phi}_1\otimes\widetilde{N}_g - \widetilde{N}_g + 2\pi N_0\delta(\omega)\qquad(7A)$$

and

$$\widetilde{N}_s = 2\pi N_0\delta(\omega) - \widetilde{N}_g,\qquad(7B)$$

where $\overline{\phi}_1 = \overline{\phi}_1(\mathbf{r},t) = \int_{4\pi}\phi_1 d\Omega$ is the intensity [$cm^{-2}\ s^{-1}$] of the excitation light.

For time–harmonic excitation, that is, $\widetilde{\overline{\phi}}_1 = 2\pi\phi_1^0[\delta(\omega)+\eta\delta(\omega-\omega_0)]$, where η is the modulation, Eq. (7) can be solved using the following approximations. When the saturation level is not significant, i.e., $N_g \approx N_0$, we have

$$\widetilde{N}_g(0) = 2\pi N_0\left(1 - \tau\Sigma_{T,1\rightarrow2}\phi_1^0\right)\delta(0),\qquad(8)$$

$$\widetilde{N}_s(\omega_0) = -\widetilde{N}_g(\omega_0) = \frac{2\pi\tau\Sigma_{T,1\rightarrow2}N_0\phi_1^0\eta}{1 + j\omega_0\tau}\delta(0).\qquad(9)$$

When the saturation level is more significant, the coupling between DC and the fundamental frequency and its first overtone should be considered, but the contributions of higher–order harmonics can be ignored, permitting the following approximations:

$$\widetilde{N}_g(0) = \frac{2\left(1+\tau\Sigma_{T,1\rightarrow2}\phi_1^0\right)^2 + 2\left(\omega_0\tau\right)^2}{2\left(1+\tau\Sigma_{T,1\rightarrow2}\phi_1^0\right)^2 + 2\left(\omega_0\tau\right)^2 - \left(\tau\Sigma_{T,1\rightarrow2}\varepsilon\phi_1^0\right)^2}$$

$$\times\frac{2\pi N_0}{1+\tau\Sigma_{T,1\rightarrow2}\phi_1^0}\delta(0)\qquad(10)$$

$$\tilde{N}_g(\omega_0) = \frac{-\tau\Sigma_{T,1\to2}\phi_1^0\eta\left(1+\tau\Sigma_{T,1\to2}\phi_1^0 - j\omega_0\tau\right)}{2\left(1+\tau\Sigma_{T,1\to2}\phi_1^0\right)^2 + 2\left(\omega_0\tau\right)^2 - \left(\tau\Sigma_{T,1\to2}\phi_1^0\eta\right)^2}$$

$$\times \frac{2\pi N_0}{1+\tau\Sigma_{T,1\to2}\phi_1^0}\delta(0) = -\tilde{N}_s(\omega_0) \qquad (11)$$

The goal of the inverse problem is to solve equation (6) for $\mu_{T,1\to2}$, γ, and τ under different source and detection conditions. This requires two reconstruction steps. In the first step, we solve for the background absorption and scattering coefficients, μ_a and μ_s, of the medium at the excitation and the emission wavelengths, using previously developed techniques [9]. The second step is to reconstruct $\mu_{T,1\to2}$, γ, and τ with estimates of $\tilde{\phi}_1$ and $\tilde{\phi}_2^+$ that were calculated numerically using the coefficients obtained from the first step. The following are two proposed methods for this second step.

(A) DC source

If we use DC sources, then equation (6) becomes

$$\tilde{R} = \int_V \frac{\tilde{\phi}_1\tilde{\phi}_2^+}{4\pi}\left(\gamma N_0\Sigma_{T,1\to2}\right)d^3r = \int_V w\left(\gamma N_0\Sigma_{T,1\to2}\right)d^3r, \quad (12)$$

where $w \equiv w_{DC} = \tilde{\phi}_1\tilde{\phi}_2^+/4\pi$ is the weight function. If $\tilde{\phi}_1$ and $\tilde{\phi}_2^+$ can be precalculated assuming that lumiphore is not present, then the unknown quantity $\gamma N_0\Sigma_{T,1\to2}$ can be computed by solving a linear system obtained by discretizing (12). Furthermore, if $\Sigma_{T,1\to2}$ is known, γN_0 can be obtained. Here, only the product of quantum efficiency and lumiphore concentration is found, and they can not be directly separated.

(B) AC source

If modulated sources are used and γN_0 is solved for by analyzing the DC component of the response as described above and we adopt the approximation in Eq. (9), then equation (6) becomes

$$\tilde{R} = \int_V w\frac{1-j\omega_0\tau}{1+\omega_0^2\tau^2}d^3r, \qquad (13)$$

where $w \equiv w_{AC} = \gamma\Sigma_{T,1\to2}N_0\tilde{\phi}_1\tilde{\phi}_2^+/4\pi$. Equation (13) can be discretized, and the real and imaginary parts of the detector readings give rise to two distinct systems of linear equations, from which the real part, $1/\left(1+\omega_0^2\tau^2\right)$, the imaginary part, $-\omega_0\tau/\left(1+\omega_0^2\tau^2\right)$, and their ratio, $-\omega_0\tau$, can be reconstructed. Because ω_0 is known, τ can also be deduced. If the approximation in Eq. (7) is adopted, we get

$$\tilde{R} = \int_V w\frac{1}{1+\tau\Sigma_{T,1\to2}\phi_1^0} \times$$

$$\frac{2\left(1+\tau\Sigma_{T,1\to2}\phi_1^0 - j\omega_0\tau\right)}{2\left(1+\tau\Sigma_{T,1\to2}\phi_1^0\right)^2 + 2\left(\omega_0\tau\right)^2 - \left(\tau\Sigma_{T,1\to2}\phi_1^0\eta\right)^2}d^3r \quad (14)$$

where w is the same as that in Eq. (13). When $\tau\Sigma_{T,1\to2}\phi_1^0 \ll 1$, Eq. (14) reduces to Eq. (13).

3. Simulations and Experiments

Simulations

Analytic solutions of a 3-D diffusion equation were used to compute the detector readings and weight functions for reconstruction. Figure 1 illustrates the phantom structure where a 10.0 cm×10.0 cm×0.5 cm square region of interest (ROI) in an infinite medium was defined. The ROI and the surrounding medium have both the same scattering cross section and absorption cross sections, that is, $\mu_{s1} = \mu_{s2} = 1\,\text{mm}^{-1}$ and $\mu_{a1} = \mu_{a2} = 0.01\,\text{mm}^{-1}$. The diffusion constant and diffusion length for this medium are, respectively, 0.33 mm and 5.74 mm. Lumiphores were distributed in a central 3.0 cm×3.0 cm×0.5 cm volume of the ROI (Figure 1B), with $\mu_{T,1\to2} = 0.00001\,\text{mm}^{-1}$. Sources were located every 10 degrees on a circle of 10 cm diameter about the center of the ROI. For each source, thirty nine detectors positioned every nine degree on the same circle were used to collect emitted photons. Two frequencies – DC and 100 MHz – were simulated in order to generate required information for both $\gamma\mu_{T,1\to2}$ and mean lifetime reconstructions, as described in Eqs. (12), (13), and (14).

(A)

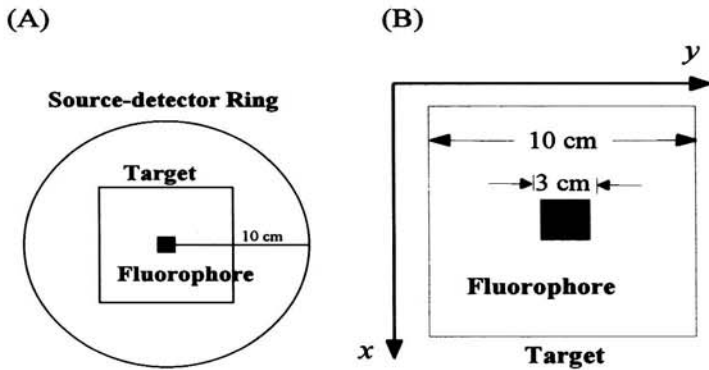**Source-detector Ring**

Figure 1. Illustration of phantom structure and source-detector ring used in simulation.

(A)

(B)

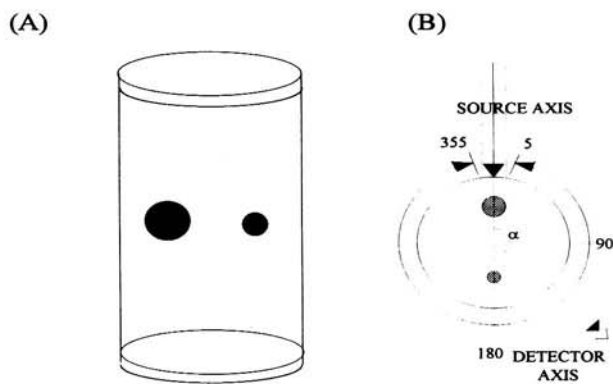Figure 2. (A) Tissue phantom for the experiment, where two balloons were suspended in the cylinder; (B) Source and detector configurations.

Experiment

The experimental tissue phantoms are sketched in Figure 2A, and the source and detector configurations in Figure 2B. Two balloons containing different volumes (0.8 and 1.2 mL) of Rhodamine 6G dye at a concentration of ~50 µM were embedded in an 8-cm-diameter cylindrical phantom filled with 0.2% Intralipid® (% lipid per unit volume). There was no added dye in the background medium. A 0.75W, multi-line (average wavelength ~490 µm) argon laser source was used to irradiate the phantom. A filter blocked excitation light from entering the detector. The detector was a Hamamatsu C3140 CCD camera directed normal to the phantom to collect the emission light. A limited illumination angle was used. The detectors were located at 30° on the border of the cylinder, and the source was positioned at 10° from 90° to 150° counterclockwise relative to the source. The source intensity was recorded for each measurement using a Coherent Labmaster-E. Each measurement was then corrected for the dark current, source intensity, and lens aperture. At least two measurements were taken and averaged to obtain the detector readings for each source-detector pair.

The optical thickness of the phantom medium was ~40 transport mean free pathlengths, both the excitation and emission wavelength. Weight functions for the corresponding reference media were computed by Monte Carlo simulations assuming an optical thickness of 20 transport mean free paths.

Image Reconstruction

Image reconstructions were performed using the CGD method with a rescaling technique and positivity constraints [10]. 2-D reconstructions based on the simulation data were performed in the x-y plane of the ROI (Figure 1B). The targets were sampled every 5 mm in either the x- or y-direction, which corresponds to 21×21 or 441 voxels. In the experimental-data case, the reconstructions (Figure 3A) were performed by assuming symmetry along the z-axis, and the weights of voxels with the same z-coordinate were summed to obtain an integrated value. Only the central planes of the reconstruction results are displayed. Figure 3B illustrates the cylindrical coordinate system, where the ρ- and ϕ- coordinates are shown in the figure and the z-coordinate is normal to the plane of the figure. There are 400 voxels in each plane.
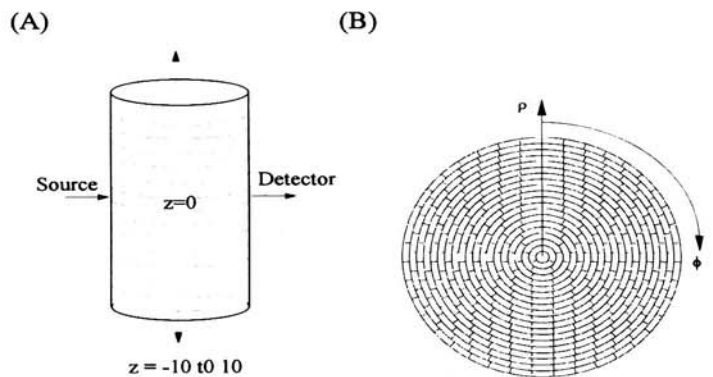
(A)   (B)

Figure 3. (A) 2-D reconstruction, for which translational invariance along the z-axis is assumed, The cylindrical coordinate system used to discretize the phantom is shown in (B).

The reconstructed $\gamma N_0 \Sigma_{T,1 \to 2}$ was also used to guide the mean lifetime reconstruction. In this technique, a "concentration correction" was adopted to make additional use of the concentration information. The maximum value of the $\gamma N_0 \Sigma_{T,1 \to 2}$ map was first obtained and any value less that 0.01 times this was set

to zero. This corrected $\gamma N_0 \Sigma_{T,1\to 2}$ map was then used in the calculation of the weight matrix for the mean lifetime reconstructions.

4. Results

Figure 4 shows reconstructed images of the product of lumiphore concentration, microscopic cross section, and quantum yield from simulated data at the DC frequency after (A) 10, (B) 100, (C) 1,000 iterations, using the CGD method, and the target is sketched in (D). Figure 5 shows the reconstructed mean lifetime for the same target medium. Figure 6 shows the reconstruction results obtained from the experimental data, using the CGD method, after (A) 10, (B) 100, (C) 1,000, (D) 10,000 iterations; the target is shown in (E).

5. Discussion and Conclusions

The size and location of $\gamma\mu_{T,1\to 2}$ are successfully reconstructed, as shown in Figure 4. The structure of the target, however, is less satisfactory since its central region is missing. Comparing Figures 4A, 4B and 4C, we see that this error increases with the number of iterations. This may be caused by the large gradient in the weight function, wherein the central voxels have the smallest weights so their contributions to the detector response is overshadowed by those of the surrounding

voxels. The same phenomenon was also observed in the mean lifetime reconstruction (Figure 5). The spatial extent of the reconstructed τ is a little larger than that of the reconstructed $\gamma\mu_{T,1\to 2}$. This is because the reconstruction of τ requires additional processing, involving reciprocation of the real and/or imaginary parts of Eq. (13). Since the real and/or imaginary part in some voxels that should be zero are set instead to a very small nonzero number, those voxels may make significant contribution to the reconstruction of τ even if there is no lumiphore actually present in them.

Inspection of the results from the experimental data (Figure 6) shows that the two balloons are located, and artifacts are present on the boundary. The two inhomogeneities are about the same size but with different intensities, which roughly coincides with the difference in balloon volume. This indicates a non–uniqueness between size and intensity, which is usually a consequence of underdeterminedness and/or ill–posedness of the imaging operator. The conditioning of the imaging operator is a function of the number and location of source–detector pairs, and the size and physical properties of the target medium. In general, more source–detector pairs are needed to decrease underdeterminedness; however, improperly located source–detector pairs may not lead to any improvement at all. In addition, constraints derived from *a priori* information about the target media, *e.g.*,
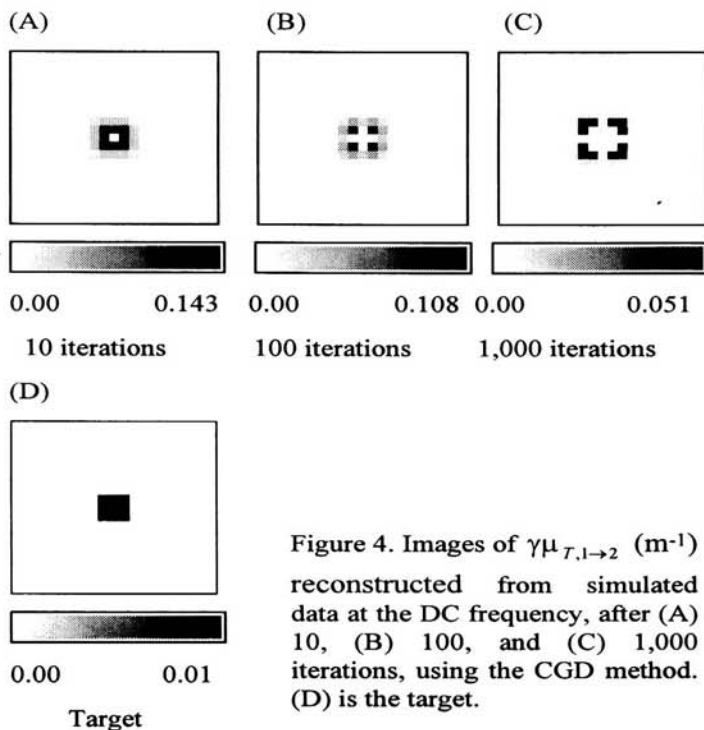

Figure 4. Images of $\gamma\mu_{T,1\to 2}$ (m⁻¹) reconstructed from simulated data at the DC frequency, after (A) 10, (B) 100, and (C) 1,000 iterations, using the CGD method. (D) is the target.
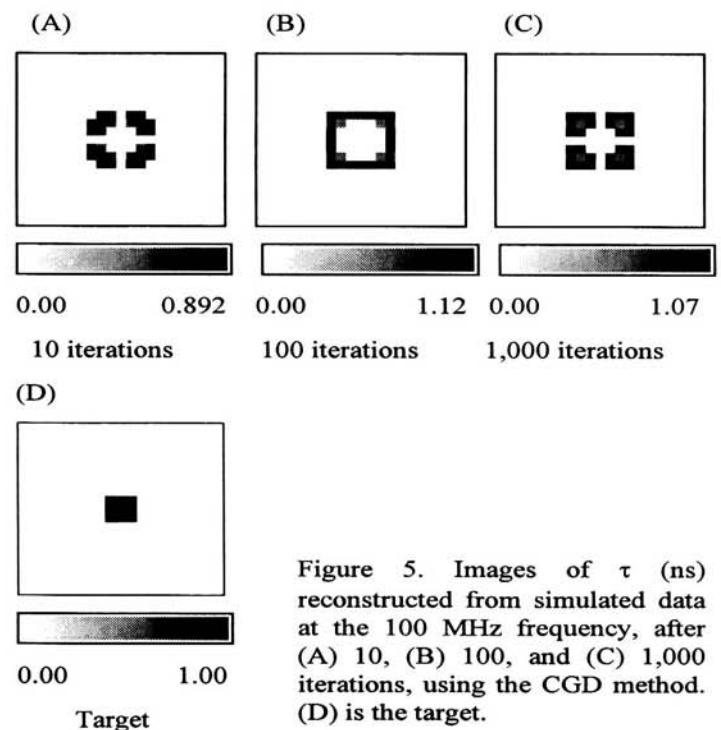

Figure 5. Images of τ (ns) reconstructed from simulated data at the 100 MHz frequency, after (A) 10, (B) 100, and (C) 1,000 iterations, using the CGD method. (D) is the target.

(A)　(B)　(C)

10 iterations　100 iterations　1,000 iterations
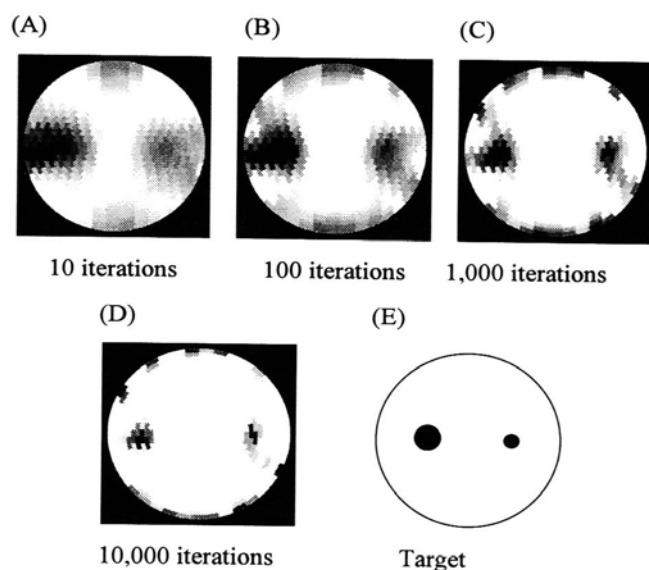
(D)　(E)

10,000 iterations　Target

Figure 6. Reconstruction results obtained from the experimental data, using CGD method, after (A) 10 iterations, (B) 100 iterations, (C) 1,000 iterations, and (D) 10,000 iterations. The target is shown in (E).

the positivity constraint adopted in this study, should be used to help guide the reconstructions.

6. Acknowledgment

7. References

1.　*Medical Optical Tomography: Functional Imaging and Monitoring*, G. Müller *et al.*, eds., SPIE Institutes vol. IS11, SPIE Press, Bellingham, WA, 1993.

2.　*OSA Proceedings on Advances in Optical Imaging and Photon Migration*, R. R. Alfano, ed., vol. 21, Optical Society of America, Washington, DC, 1994.

3.　J. Chang, H. Graber, R. Aronson, and R. L. Barbour, "Fluorescence imaging using transport–theory–based imaging operators," in *Proc. of the 17th Annual IEEE EMBS International Conference*, (Montreal), Sep. 1995.

4.　J. Chang, R. L. Barbour, H. Graber, and R. Aronson, "Fluorescence optical tomography," in *Proc. Experimental and Numerical Methods for Solving Ill-Posed Inverse Problems: Medical and Nonmedical Applications*, vol. SPIE-2570, (San Diego), 1995.

5.　M. A. O'Leary, D. A. Boas, X. D. Li, B. Chance, and A. G. Yodh, "Fluorescence lifetime imaging in turbid media," Optics Letters, vol. 21, pp. 158–160, January 1996.

6.　P. E. Gill, W. Murray, M. H. Wright, *Practical Optimization*, New York: Academic Press, 1981.

7.　*Conceptual Basis for Calculations of Absorbed–Dose Distribution*, NCRP Report No. 108, 1991.

8.　H. C. van de Hulst, *Multiple Light Scattering: Tables, Formulas, and Applications*, vol. 1, chap. 3, Academic Press, New York, NY, 1980.

9.　J. Chang, R. Aronson, H. L. Graber, R. L. Barbour, "Imaging diffusive media using time-independent and time-harmonic sources: dependence of image quality on imaging algorithms, target volume, weight matrix, and view angles," vol. SPIE–2389, (San Jose), Feb. 1995.

10.　J. Chang, H. L. Graber, R. L. Barbour, "Image reconstruction of dense scattering media from CW sources using constrained CGD and a matrix rescaling technique," vol. SPIE–2389, (San Jose), Feb. 1995.